

Energy, Environmental, and Catalysis Applications

## Enhancing the Performance of Self-standing Si/ PCNF Anode by Optimizing the Porous Structure

Xiaoqiang tian, Qi Xu, Li Cheng, Leixin Meng, Heng Zhang, Xiaofeng Jia, Suo Bai, and Yong Qin

*ACS Appl. Mater. Interfaces*, **Just Accepted Manuscript** • DOI: 10.1021/acsami.0c05658 • Publication Date (Web): 27 May 2020

Downloaded from pubs.acs.org on May 27, 2020

### Just Accepted

"Just Accepted" manuscripts have been peer-reviewed and accepted for publication. They are posted online prior to technical editing, formatting for publication and author proofing. The American Chemical Society provides "Just Accepted" as a service to the research community to expedite the dissemination of scientific material as soon as possible after acceptance. "Just Accepted" manuscripts appear in full in PDF format accompanied by an HTML abstract. "Just Accepted" manuscripts have been fully peer reviewed, but should not be considered the official version of record. They are citable by the Digital Object Identifier (DOI®). "Just Accepted" is an optional service offered to authors. Therefore, the "Just Accepted" Web site may not include all articles that will be published in the journal. After a manuscript is technically edited and formatted, it will be removed from the "Just Accepted" Web site and published as an ASAP article. Note that technical editing may introduce minor changes to the manuscript text and/or graphics which could affect content, and all legal disclaimers and ethical guidelines that apply to the journal pertain. ACS cannot be held responsible for errors or consequences arising from the use of information contained in these "Just Accepted" manuscripts.

Enhancing the Performance of Self-standing  
Si/PCNF Anode by Optimizing the Porous Structure

*Xiaoqiang Tian,<sup>†</sup> Qi Xu,<sup>‡</sup> Li Cheng,<sup>†</sup> Leixin Meng,<sup>†</sup> Heng Zhang,<sup>†</sup> Xiaofeng Jia,<sup>†</sup> Suo  
Bai<sup>\*†</sup> and Yong Qin<sup>\*†</sup>*

<sup>†</sup> Institute of Nanoscience and Nanotechnology, Lanzhou University, Lanzhou, 730000,  
China.

<sup>‡</sup> School of Advanced Materials and Nanotechnology, Xidian University, Xi'an, 710071,  
China.

**KEYWORDS:** silicon anode, electrospinning, carbon nanofiber, porous structure, lithium  
ion battery

**ABSTRACT**

Embedding silicon nanoparticles into carbon nanofiber is one of the effective methods to fabricate a self-standing and binder-free Si-based anode material for lithium ion battery. However, the sluggish Li ion transport limits the electrochemical performance in the regular strategies, especially in high rate condition. Herein, a kind of silicon nanoparticles in porous carbon nanofiber structure (Si/PCNF) has been fabricated through facile electrospinning and subsequent thermal treatment. By adjusting the mass ratio to 0.4: 1, a Si/PCNF anode material with effective Li<sup>+</sup> migration pathway and excellent structural stability can be obtained, resulting in an optimal electrochemical performance. Although increasing the mass ratio of PEG to PAN further can lead to a larger pore size and beneficial to the Li<sup>+</sup> migration and thus profitable for the rate capacity, the structural stability will get worse at the same time as more defect will formed and lead to a weaker C-C binding and thus decrease the cycling stability. Remarkably, the rate capacity reaches 1033.4 mAh g<sup>-1</sup> at the current density of 5 A g<sup>-1</sup>, and the cycling capacity is 933.2 mAh g<sup>-1</sup> at 0.5 A g<sup>-1</sup> after 200 cycles keeping a retention rate of 80.9% with an initial coulombic efficiency (ICE) of 83.37%.

## INTRODUCTION

Nowadays, the power supply of most portable electronic devices such as mobile phones, laptops and electric vehicles (EVs) is provided by the rechargeable lithium ion batteries (LIBs), which need long endurance and high power density to ensure the working time and shorten the charging period.<sup>1-7</sup> Tremendous efforts have been made to improve the abovementioned performance to meet the practical application. Silicon (Si) attracts lots of researchers' attention because it occupies ultrahigh theoretical discharge capacity (3579 mAh g<sup>-1</sup>) among all the anode candidates and moderate discharge potential ( $\sim 0.5$  V *vs.* Li<sup>+</sup>/Li).<sup>8,9</sup> However, the intrinsic deficiencies such as relatively low electronic conductivity ( $\sim 10^{-3}$  S·cm<sup>-1</sup>)<sup>10</sup> and large volume variation beyond 300%<sup>11,12</sup> during lithiation process confine its practical application, and the continuous consumption of Li<sup>+</sup> by repeatedly generating of solid electrolyte interphase (SEI) in the interface between Si and electrolyte causes the rapid decay of LIBs' Li-storage performance.

Depending on a previous study result that below the critical size of  $\sim 150$  nm did no cracking occur<sup>13</sup>, reducing the size of Si into nanoscale is one of the effective strategies

1  
2  
3  
4 to alleviate mechanical stress under Li-Si alloying status<sup>14-18</sup>. Further, compositing nano-  
5  
6  
7 sized Si with carbonaceous material can enhance its electrochemical performance owing  
8  
9  
10 to the increase of electrical conductivity and the separation of active Si from electrolyte  
11  
12  
13 avoiding supererogatory formation of SEI<sup>12,19,20</sup>. A self-supporting structure that  
14  
15  
16 embedding Si nanoparticles (NPs) in carbon nanofiber (CNF) using a facile  
17  
18  
19 electrospinning<sup>21-23</sup> and subsequent calcination method has been adopted for anode  
20  
21  
22 materials, which avoids the extra conductive additives and insulating binder. Later, more  
23  
24  
25 efforts have been made to improve the performance of Si/CNF-based anode materials,  
26  
27  
28 for instance, adding polyethylene glycol or TiO<sub>2</sub> as a dispersion agent to weaken the  
29  
30  
31 aggregation of Si NPs in the CNF matrix<sup>24,25</sup>, creating nanocavity around Si NPs as the  
32  
33  
34 interspace to release the volume expansion<sup>26,27</sup> and creating porous structure in Si/CNF  
35  
36  
37 matrix to further improve both the cycling and rate capacities. For the introduction of  
38  
39  
40 porous structure, the volume expansion of Si NPs during lithiation process can be  
41  
42  
43 accommodated by the adjacent pores, the contact interface between electrolyte and  
44  
45  
46 active material can be increased due to the large surface of porous structure, and more  
47  
48  
49 importantly, the transport pathway of Li<sup>+</sup> reacting with Si can be shortened enormously.  
50  
51  
52  
53  
54  
55  
56  
57  
58  
59  
60

Based on the advantages mentioned above, a Meso-C/Si-CNF structure had been fabricated and exhibited excellent cycling stability ( $1140 \text{ mAh g}^{-1}$  at  $0.1 \text{ A g}^{-1}$  after 100 cycles) and high rate capability ( $969 \text{ mAh g}^{-1}$  at  $2 \text{ A g}^{-1}$ )<sup>28</sup>. However, the extra carbon skin decreased the mass ratio of Si and limited  $\text{Li}^+$  transport.

Herein, a new anode material composed of silicon nanoparticles in porous carbon nanofiber structure (Si/PCNF) has been fabricated, and its electrochemical performance is enhanced by optimizing porous structure through controlling the mass ratio of polyethylene glycol (PEG) in the electrospinning precursor. When the mass ratio of PEG to polyacrylonitrile (PAN) is adjusted to 0.4:1, the high reversible capacity reaches  $933.2 \text{ mAh g}^{-1}$  at  $0.5 \text{ A g}^{-1}$  after 200 cycles keeping a retention rate of 80.9% with an ICE of 83.37%, and the optimal rate capacity is  $1033.4 \text{ mAh g}^{-1}$  at the current density of  $5 \text{ A g}^{-1}$ .

## RESULTS AND DISCUSSIONS

As shown in **Figure 1a**, the enhancement of electrochemical performance can be attributed to the relatively stable CNFs substrate and the favorable diffusion pathway of  $\text{Li}^+$  from the porous structural Si/CNF-based anode material. The porous structure can

supply a fast  $\text{Li}^+$  pathway to ensure the Li-Si alloying process and lead to a high rate capacity. The mass loss of Si/PAN and Si/PAN/PEG in air is evaluated by TGA and shown in Figure 1b. Compared with Si/PAN, Si/PAN/PEG has an evident mass loss in the range of 130-180 °C, which can be attributed to the oxidative decomposition of PEG to produce  $\text{CO}_x$  and  $\text{H}_2\text{O}$ , and the formation of porous structure occurs in this stage. The phenomena of synchronously mass decrease of Si/PAN and Si/PAN/PEG with the increase of temperature is mainly ascribed to the partial decomposition of PAN. Eventually, as shown in **Figure S1**, the 56.9 wt% mass ratio of Si in the as-prepared Si/PCNF because Si NPs are the only residuum after thermogravimetric process at 600 °C (**Figure S2**), indicates a theoretical capacity of 2196.8 mAh g<sup>-1</sup>. Porous structure is further characterized by the  $\text{N}_2$  sorption as shown in Figure 1c, the result suggests the pores in Si/PCNF distributes with a diameter within 1~2 nm. It is expected that the structure can shorten the transport pathway of  $\text{Li}^+$  to enhance the redox reactivity of Si NPs, especially at high current density, and buffer the volume expansion during the lithiation process. The appearance of macropore of nearly 10 nm and mesopore extending to 100 nm both in Si/PCNF and

Si/CNF is attributed to the space between fibers, which ensures the full infiltration of matrix fibers with electrolyte.

The Si/PCNF film with a uniform thickness of 65  $\mu\text{m}$  is obtained (**Figure 2a**) and Si NPs are embedded in continuous CNF with a typical diameter of  $\sim 200$  nm forming a nodular-like structure (inset in **Figure 2a** and **Figure S3**). Compared to Si/PCNF, the diameter of electrospun fiber and the fiber after peroxidation are 250 nm and 210 nm, respectively (**Figure S4**). The decrease of diameter with the heat treatment is attributed to the loss of H, O and N elements in peroxidation process and ordered arrangement of C atoms at the carbonization stage. XRD patterns of Si/PCNF and Si/CNF are shown in **Figure 2b**. The characteristic peaks around  $28.4^\circ$ ,  $47.3^\circ$ ,  $56.1^\circ$ ,  $69.1^\circ$  and  $76.4^\circ$  of  $2\theta$  degrees correspond to the (111), (220), (311), (400) and (331) diffraction planes of diamond cubic Si (JCPDS No. 27-1402), respectively. For Si/CNF, a broad peak near  $23.4^\circ$  is attributed to the C matrix from carbonized PAN with the larger interplanar of 0.38 nm (based on the Bragg formula). Si NPs are aggregated slightly and coated by a layer of C, which has a thickness of  $\sim 10$  nm (**Figure 2c-d**). The size of the micropores in CNF



matrix is too small to be exhibited in TEM images. It is proved that a larger  $d_{002}$  of C can facilitate the diffusion and storage of  $\text{Li}^+$ .<sup>29</sup> Remarkably, while the intensity of the diffraction peak of Si is normalized, the carbonic peak in Si/PCNF is weaker than that in Si/CNF, suggesting that the existence of porous structure gives rise to the smaller graphitic microcrystallines.

The influence of porous structure in Si/CNF-based electrode on the electrochemical property is shown in **Figure 3**. CV curves of Si/PCNF anode are exhibited in **Figure S5**, indicating the typical electrochemical reaction processes of Si. Under a current density of  $0.5 \text{ A g}^{-1}$ , Si/PCNF electrode shows a higher cycling stability than Si/CNF' during the cycling process, and the ICE is increased from 75.26% to 83.37% (inset in Figure 3a). The enhanced ICE is higher than other reported Si/CNF-based anode materials, shown in **table S1**. The improvement of rate capacity for Si/PCNF electrode is shown in Figure 3b, with the increase of current density, higher capacities are obtained from Si/PCNF electrode, suggesting a high rate performance benefiting from the porous structure.

The overpotentials (originated from median potential) of Si/CNF and Si/PCNF electrodes are obtained from charge/discharge profiles, as shown in Figure 3c. At the current density of 5.0 A g<sup>-1</sup>, the overpotential of Si/CNF electrode is 0.791 V, in contrast, for Si/PCNF ones, the value is only 0.479 V. Meanwhile, we found the diameter and density of micropore are increasing with the mass ratio of PEG (Figure 1c). It is evident that the electrochemical kinetics of Si/PCNF electrodes can be facilitated by the condition of pore because they play the role of transport channels for Li<sup>+</sup> in the cycling process, especially at high rates. Further, relative Li<sup>+</sup> diffusion coefficient (D) of two electrodes are evaluated by CV curves (see **Figure S6**) to investigate the porous structure on Si/CNF electrode. Based on Randles-Sevcik equation (Eq 1), peak current ( $i_p$ ) is the function of scan rates ( $\nu$ ).

$$i_p = 0.4663nF\sqrt{\frac{nFD}{RT}}AC\sqrt{\nu} \quad (1)$$

Where  $n$ ,  $F$ ,  $R$  and  $T$  are the charge transfer number, Faraday constant, gas constant and temperature, respectively,  $A$  and  $C$  are the active electrode area and concentration of lithium ion, respectively. The linearity is established and the fitted slope of the curve

belongs to the relationship between  $i_p$  and  $u^{1/2}$ , as shown in Figure 3d. The relatively high value of 10.95 obtained from Si/PCNF-0.40 electrode is higher than 6.52 from Si/CNF electrode, suggesting that the porous structural electrode possesses a higher D owing to the suitable diffusion pathway of  $\text{Li}^+$ .

To further study the influence of porous structure on the electrochemical property, a series of Si/PCNF electrodes are fabricated by controlling the mass ratio of PEG and the properties are evaluated, where 0.25 g, 0.33 g, 0.40 g, 0.50 g and 0.55 g are mixed with 1 g PAN and 0.5 g Si NPs, named Si/PCNF-0.25, -0.33, -0.40, -0.50 and -0.55, respectively. As shown in **Figure 4a**, at the current density of  $0.2 \text{ A g}^{-1}$ , Si/PCNF-0.40 electrode shows the highest reversible capacity of  $1260.2 \text{ mAh g}^{-1}$  after 120 cycles with a capacity retention ratio of 76.1% and excellent ICE of 84.46% (inset in Figure 4a). The high ICE can be ascribed to the open pore structure, which facilitates the participation of more  $\text{Li}^+$  in the electrochemical reaction rapidly<sup>30</sup>. When the current density is increased to  $0.5 \text{ A g}^{-1}$ , as shown in Figure 4b, although the high ICE over 80% are obtained for every electrode (insert in Figure 4b), the difference in capacity retention for the electrodes are

more evident and Si/PCNF-0.40 shows the highest capacity of 933.2 mAh g<sup>-1</sup> after 200 cycles with a retention ratio of 80.9%. The distinct differences of long cycle life for Si/PCNF-0.40 imply a high stability in electrochemical reaction process.

The rate capacities for the Si/PCNF electrodes are evaluated at a series of current density. As shown in Figure 4c, the highest reversible capacity of 1033.4 mAh g<sup>-1</sup> for Si/PCNF-0.40 electrode at 5 A g<sup>-1</sup> can be obtained. As shown in Figure 4d, the rate capacities at relatively low current densities (0.1, 0.2, 0.5 and 1 A g<sup>-1</sup>) are approximate for different electrodes except for the outstanding performance of Si/PCNF-0.40 with the increase of current density (2 and 5 A g<sup>-1</sup>). This phenomenon is further investigated by overpotential, when the current density increases from 0.1 to 5 A g<sup>-1</sup>, the charge/discharge profiles vary with the mass ratio of PEG to PAN, as shown in Figure S7. The overpotentials are smaller and almost unchanged at 0.1 A g<sup>-1</sup> for every electrode, while the smallest values of 337 and 445 mV are found in Si/PCNF-0.40 electrode compared with other Si/PCNFs' at 2 and 5 A g<sup>-1</sup>, respectively (Figure 4f and Table S2), indicating the smallest value of voltage hysteresis at high current rates<sup>31,32</sup>.

We also find that the electrochemical property of Si/PCNF electrodes deteriorates when further increase of the mass ratio of PEG. To understand this phenomenon, Nyquist plots of pristine and after 120 cycles of Si/PCNF-0.40 and Si/PCNF-0.55 are measured, respectively, shown in **Figure 5a-b** (the corresponding equivalent circuit is shown in **Figure S8**). Evidently, in Figure 5a, the rising values from 76 to 148  $\Omega$  of Si/PCNF-0.40 suggest that the electrode is relatively stable during electrochemical reactions, which is attributed to the synergistic effect of appropriate pathway for  $\text{Li}^+$  diffusion and firm framework structure for electron transferring. However, a drastic increase of impedance from 66 to 325  $\Omega$  in Si/PCNF-0.55 electrode (Figure 5b), indicates an inferior ability to maintain the stability of electrode during cycling process. The morphology of Si/PCNF-0.40 and Si/PCNF-0.55 after 120 cycles at  $0.5 \text{ A g}^{-1}$  is checked to further reveal the capacity fading (Figure 5c-d). Compared with the unreacted electrode (Figure 1b), the morphology of Si/PCNF-0.40 is almost unchanged (Figure 5c and **Figure S9**) but Si/PCNF-0.55 is severely broken after the cycling, indicating a deteriorative mechanical stability caused by the superabundant pore existing in the matrix fiber. The broken electrode leads to the

disconnection of the Si NPs from the carbon channels; thus, the electrical contact is getting worse, and a decreasing electrochemical performance is caused.

## CONCLUSIONS

By controlling the mass ratio of pore-forming agent, we successfully designed a Si/PCNF and optimized the electrochemical performance as an anode material of LIBs. As a result, the sample of Si/PCNF-0.40 exhibits an optimal rate capacity of 1033.4 mAh g<sup>-1</sup> at the current density of 5 A g<sup>-1</sup> and an excellent specific capacity of 933.2 mAh g<sup>-1</sup> at 0.5 A g<sup>-1</sup> after 200 cycles keeping a retention rate of 80.9% with a high ICE of 83.37%. The enhancement of the electrochemical performance can be attributed to the more elastic carbon fiber-based substrate and the favorable diffusion condition of Li<sup>+</sup> for the porous structural Si/CNF-based anode material.

## EXPERIMENTAL SECTION

**Preparation of Si/PCNF:** 0.25 g Si NPs (~80 nm, as shown in **Figure S10**) are soaked in 5% hydrofluoric acid for 30 min to remove their surface silica layer and then centrifuged

by dimethylformamide (DMF) for three times. Subsequently, the as-prepared Si NPs and 0.5 g PAN ( $M_w = 150,000$ ) are dissolved in 5 g DMF with 10 hours stirring at room temperature. A certain amount of PEG ( $M_w = 15,000$ ) is added into the Si/PAN/DMF solution and uniformly dispersed by fiercely stirring. The as-prepared homogeneous solution as the precursor for electrospinning is transferred to a plastic syringe with an inner needle diameter of 0.4 mm. 21 kV voltage is applied between the collecting plate and the tip of the needle and the collection distance maintains 21 cm. To ensure the optimal electrospinning condition, the ejecting rate is kept at  $0.6 \text{ mL h}^{-1}$  with the temperature and humidity of  $40^\circ\text{C}$  and 10%, respectively. The electrospun sample (Si/PAN/PEG) is dried at  $80^\circ\text{C}$  for 10 h, pre-oxidized at  $280^\circ\text{C}$  for 180 min in air and carbonized at  $900^\circ\text{C}$  for 180 min under one bar pressure in Ar with a heating rate of  $5^\circ\text{C min}^{-1}$  to enhance the electrical conductivity<sup>34</sup>. Eventually, the obtained Si/PCNF film is cut into wafer with a diameter of 10 mm acting as the anode in LIB.

**Materials characterizations:** The as-prepared Si/PCNF is investigated by field emission scanning electron microscope (FE-SEM, Apreo S, 30 kV). The crystallographic structures

of Si/PCNF are analyzed using X-ray diffraction (XRD,  $\lambda = 1.5406 \text{ \AA}$ ) system. To analyze thermal stability of PEG and calculate the mass ratio of Si to C in Si/CNF film, thermogravimetric analysis (TGA) is performed (Diamond TG/DTA) in air with a heating rate of  $5 \text{ }^{\circ}\text{C min}^{-1}$  at temperature ranging from 50 to  $700 \text{ }^{\circ}\text{C}$  for Si/PCNF and  $2 \text{ }^{\circ}\text{C min}^{-1}$  at 50 to  $380 \text{ }^{\circ}\text{C}$  for Si/PAN and Si/PAN/PEG-0.40, respectively.  $\text{N}_2$  sorption isotherms are measured at 77 K with an ASAP 2020 (Micromeritics, US), and the pore size distribution is calculated by the density functional theory (DFT) method from the adsorption branches of the isotherms.

**Electrochemical measurements:** The electrochemical performance of the Si/PCNF as anode materials in LIBs are characterized using CR 2032-type coin half cells. The wafer-like Si/PCNF film is directly used as working electrode without conductive additives and binder material, lithium foil is used as the counter/reference ones and the two parts of electrodes are separated by a separator (polypropylene (Celgard 2325)). 1 M  $\text{LiPF}_6$  in ethylene carbonate (EC) and dimethyl carbonate (DMC) mixture (1:1 v/v) act as the electrolyte. The whole assembly process is operated in an Ar-purged glove box with the



contents of H<sub>2</sub>O and O<sub>2</sub> under 1 ppm, respectively. The galvanostatic charge/discharge and rate capacity of the assembled coin cell is measured using a multi-channel battery tester (LAND, CT2001A) within the voltage range of 0.01-1.20 V (vs. Li<sup>+</sup>/Li). The cyclic voltammetry (CV) test is performed at a scan rate of 0.1 mV s<sup>-1</sup> and electrochemical impedance spectroscopy (EIS) is analyzed in the frequency range of 1-10<sup>5</sup> Hz carried by an electrochemical workstation (Chen Hua Shanghai Corp., China, CHI660E).

## FIGURES

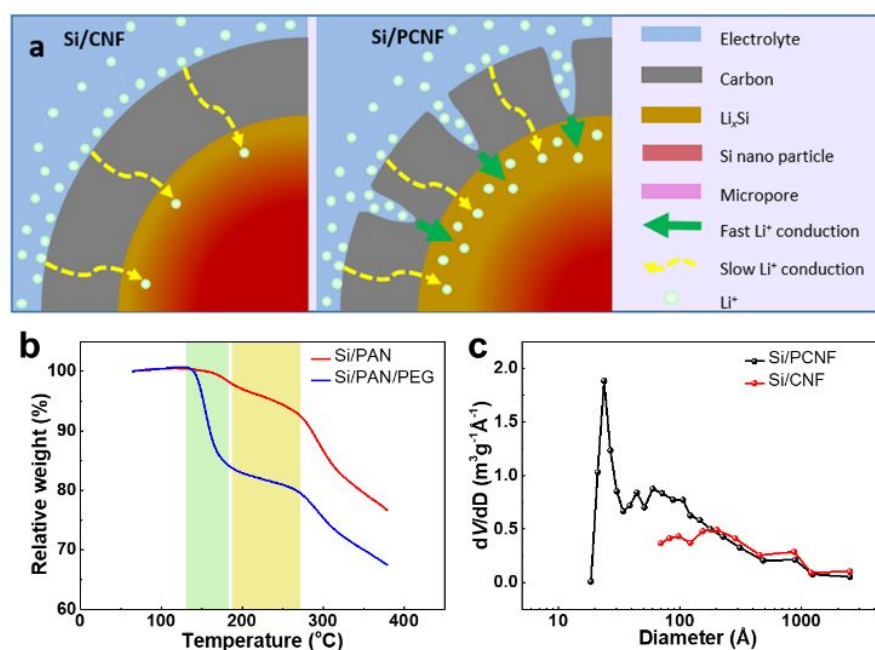


**Figure 1.** Structure and mechanism of Si/PCNF. (a) The improvement of the porous structure for the conduction of  $\text{Li}^+$ , a shorter pathway for  $\text{Li}^+$  can be supplied by the porous structure. (b) The TGA investigating of the formation process of pores, suggesting that the introduction of PEG acting as the pore-forming agent is feasible. (c) The pore size distribution varies with the introduction of pore-forming agent. Micropores are obtained by introducing PEG.

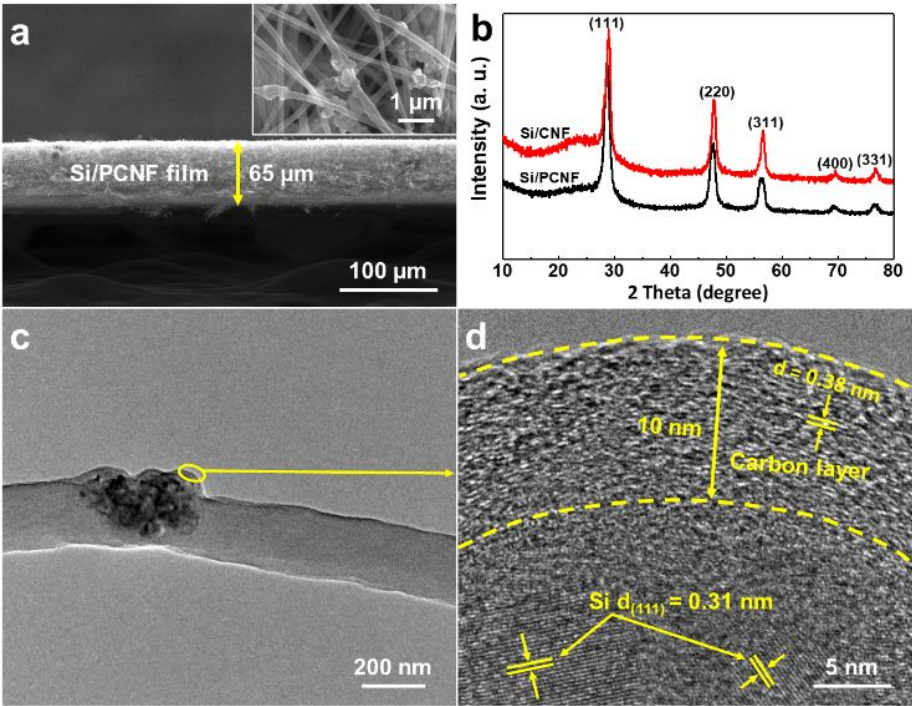


**Figure 2.** Morphology and microstructure of Si/PCNF. (a) Cross-section of SEM image of the Si/PCNF film with a uniform thickness of 65 μm (inset is the top view of the Si/PCNF

film). (b) XRD patterns of Si/PCNF and Si/CNF. (c) TEM image of Si/PCNF. Si NPs are aggregated slightly and coated by a layer of carbon. (d) High resolution TEM image shows that the crystalline silicon particle is embedded in the carbon layer with the thickness of ~10 nm.

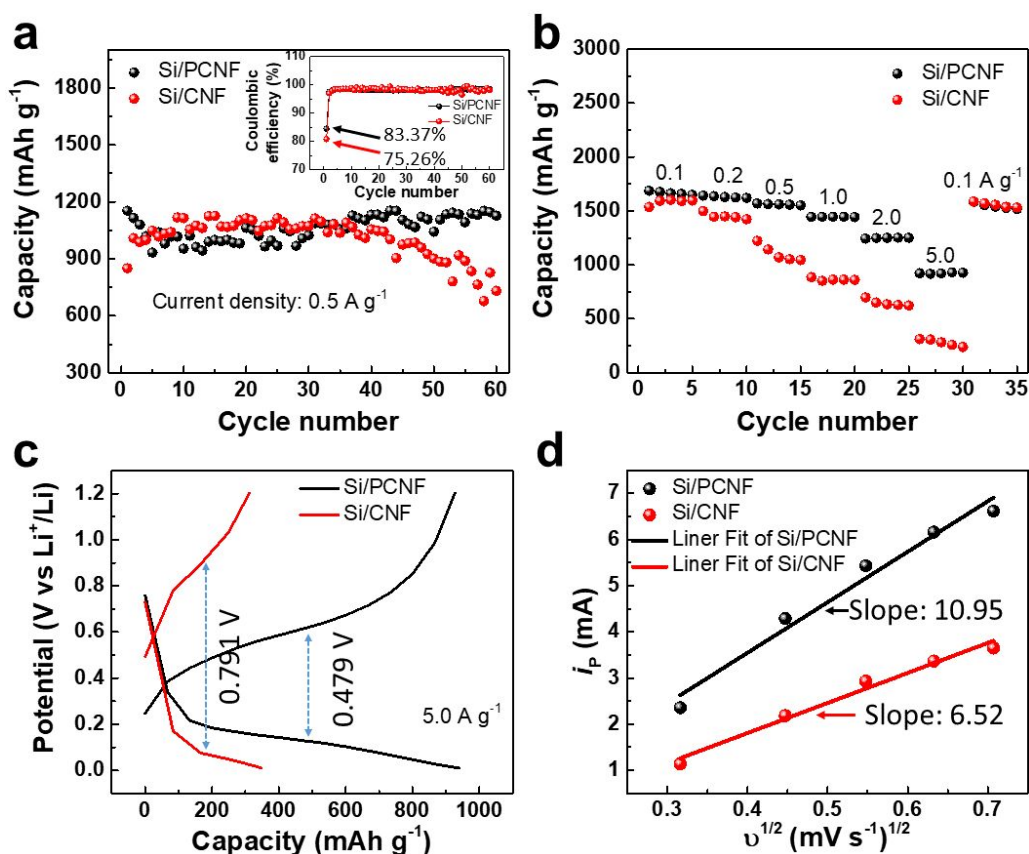


**Figure 3.** Comparison of the electrochemical properties of Si/CNF with Si/PCNF. (a) Cycling performance of the two electrodes at the current density of 0.5 A g<sup>-1</sup> (the inset is the corresponding coulombic efficiency). (b) Rate capacity of the electrodes under

different current density. A higher rate capacity is shown in Si/PCNF, especially in high current density. (c) Median potential is measured at the current density of 5 A g<sup>-1</sup>. (d) Relative Li<sup>+</sup> diffusion efficient of Si/CNF and Si/PCNF. Peak current is obtained from cyclic voltammetry curves at the scan rates of 0.1, 0.2, 0.3, 0.4 and 0.5 mV s<sup>-1</sup>.

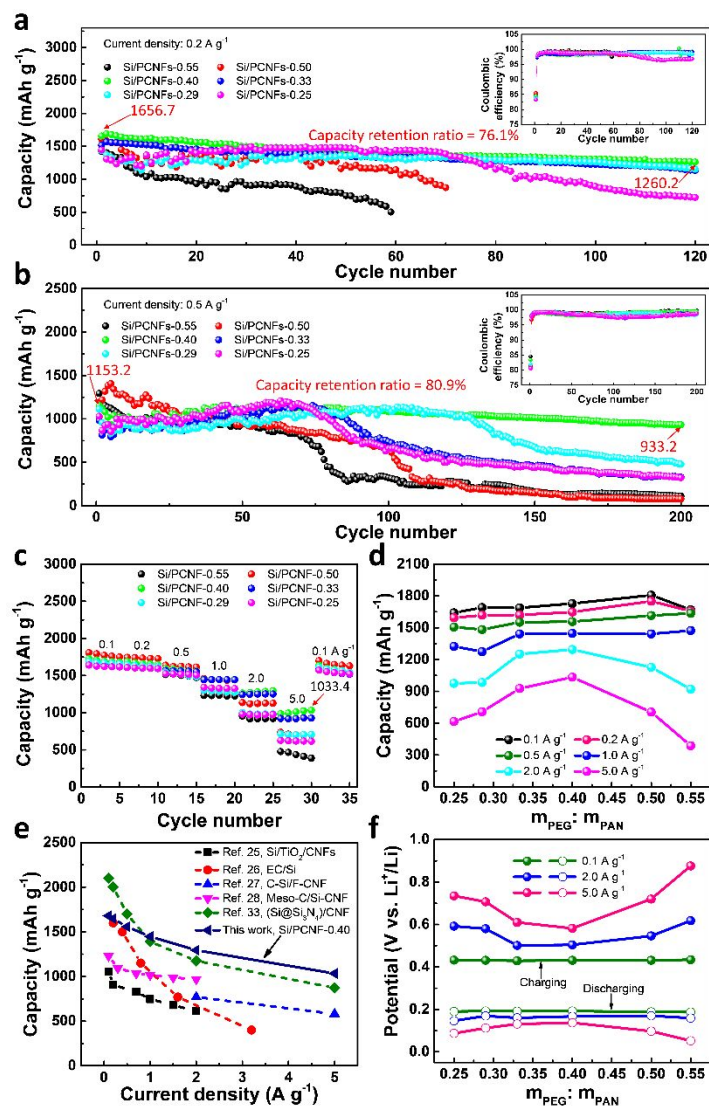


**Figure 4.** Electrochemical property of different Si/PCNF electrodes. (a) Cycling performance of Si/PCNF materials at the current densities of 0.2 A g<sup>-1</sup> and (b) 0.5 A g<sup>-1</sup>, the insets are the corresponding coulombic efficiency, individually. (c) Rate capacities and (d) Variation of the rate capacities with the mass ratio of PAN. Si/PCNF-0.40 shows the highest rate capacity when the current density is increased to 2.0 and 5.0 A g<sup>-1</sup>. (e) Comparison of the rate capacity of different reported Si/CNF-based anode materials. With the increase of current density, our Si/PCNF-0.40 shows the highest rate capacity, especially at 5.0 A g<sup>-1</sup>. (f) Median voltages of different Si/PCNF anode materials at a series of current densities.

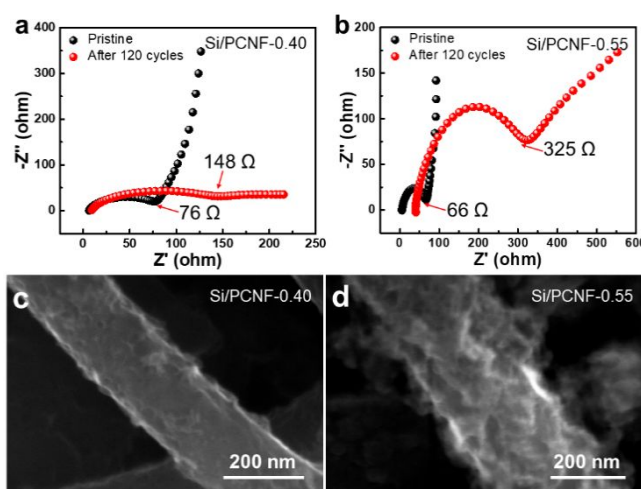


**Figure 5.** Mechanism of the deteriorating condition when the further increase of PEG. (a) EIS under pristine state and after 120 cycles of Si/PCNF-0.40 and (b) Si/PCNF-0.55. Comprising with Si/PCNF-0.40, an unstable impedance suffering from 120 cycles is shown in Si/PCNF-0.55 electrode, suggesting a poor structural stability because of excessive pore-forming agent. (c) SEM morphology of Si/PCNF-0.40 and (d) Si/PCNF-0.55 suffer from 120 cycles at the current density of  $0.2 \text{ A g}^{-1}$ .

## AUTHOR INFORMATION

### Corresponding Author

Email: [baisuo@lzu.edu.cn](mailto:baisuo@lzu.edu.cn), [qinyong@lzu.edu.cn](mailto:qinyong@lzu.edu.cn), [xuq2016@163.com](mailto:xuq2016@163.com)

### Author Contributions

The manuscript was written through contributions of all authors. All authors have given approval to the final version of the manuscript.

## NOTES

The authors declare no competing financial interest.

## ACKNOWLEDGMENT

We sincerely acknowledge the support from Joint fund of Equipment Pre-research and Ministry of Education (No. 6141A02022518), the National Program for Support of Top-notch Young Professionals, and the Fundamental Research Funds for the Central Universities (No. lzujbky-2018-ot04), NSFC (No. 81702095).

## SUPPORTING INFORMATION

Detailed experimental methods and additional explanations are included in the supporting information: Table S1 lists the electrochemical performance of various Si/CNF-based anodes. Table S2 shows the polarization potentials of Si/PCNF-based electrodes during different current densities. TGA investigation of the mass ratio of Si nanoparticles in the matrix fiber is shown in Figure S1. Figure S2 gives the evidence that Si NPs are the only residuum of Si/PCNF after thermogravimetric process at 600 °C. EDX-mapping of Si/PCNF and the elements distribution of Si and C are shown in Figure S3, respectively. Figure S4 shows the morphology and the diameter distribution of the fibers in different stages. Figure S5 is the first three cyclic voltammetry curves of Si/PCNF anode with the voltage range of 0.01-1.2 V and scan rate is 0.1 mV s<sup>-1</sup>. Figure S6 is the CV curve of Si/PCNF and Si/CNF at 0.1 to 0.5 mV s<sup>-1</sup> to calculate the relative Li<sup>+</sup> diffusion efficient. Figure S7 shows the galvanostatic charge/discharge profiles of Si/PCNF anode materials at different current densities. Figure S8 is the equivalent circuit of electrochemical impedance spectroscopy. Figure S9 is the TEM image of Si/PCNF-0.40 after 200 cycles at the current density of 0.5 A g<sup>-1</sup>. Figure S10 shows the SEM image and the diameter distribution of Si NPs we used.

## REFERENCES

- (1) Chen, D.; Lou, Z.; Jiang, K.; Shen, G. Z. Device Configurations and Future Prospects of Flexible/Stretchable Lithium-Ion Batteries. *Adv. Funct. Mater.* **2018**, 28, No. 1805596.
- (2) Susai, F. A.; Sclar, H.; Shilina, Y.; Penki, T. R.; Raman, R.; Maddukuri, S.; Maiti, S.; Halalay, I. C.; Luski, S.; Markovsky, B.; Aurbach, D. Horizons for Li-Ion Batteries Relevant to Electro-Mobility: High-Specific-Energy Cathodes and Chemically Active Separators. *Adv. Mater.* **2018**, 30, No. 1801348.
- (3) Cano, Z. P.; Banham, D.; Ye, S. Y.; Hintennach, A.; Lu, J.; Fowler, M.; Chen, Z. W. Batteries and Fuel Cells for Emerging Electric Vehicle Markets. *Nat. Energy* **2018**, 3, 279-289.
- (4) Zhou, Y.; Wang, M.; Hao, H.; Johnson, L. R.; Wang, H. W. Plug-in Electric Vehicle Market Penetration and Incentives: a Global Review. *Mitig. Adapt. Strateg. Glob. Chang.* **2015**, 20, 777-795.
- (5) Tu, F. Z.; Han, Y.; Du, Y. C.; Ge, X. F.; Weng, W. S.; Zhou, X. S.; Bao, J. C. Hierarchical Nanospheres Constructed by Ultrathin MoS<sub>2</sub> Nanosheets Braced on Nitrogen-Doped Carbon Polyhedra for Efficient Lithium and Sodium Storage. *ACS Appl. Mater. Interfaces* **2019**, 11, 2112-2119.
- (6) Guo, F.; Chen, P.; Kang, T.; Wang, Y. L.; Liu, C. H.; Shen, Y. B. Silicon-Loaded Lithium-Carbon Composite Microspheres as Lithium Secondary Battery Anodes. *Acta Phys.-Chim. Sin.* **2019**, 35, 1365-1371.
- (7) Zhao, C. Z.; Duan, H.; Huang, J. Q.; Zhang, J.; Zhang, Q.; Guo, Y. G.; Wan, L. J. Designing Solid-State Interfaces on Lithium-Metal Anodes: a Review. *Sci. China-Chem.* **2019**, 62, 1286-1299.



- (8) Huggins, R. A. Lithium Alloy Negative Electrodes. *J. Power Sources* **1999**, *81*, 13-19.
- (9) Limthongkul, P.; Jang, Y. I.; Dudney, N. J.; Chiang, Y. M. Electrochemically-Driven Solid-State Amorphization in Lithium-Silicon Alloys and Implications for Lithium Storage. *Acta Mater.* **2003**, *51*, 1103-1113.
- (10) Xu, Z. L.; Liu, X. M.; Luo, Y. S.; Zhou, L. M.; Kim, J. K. Nanosilicon Anodes for High Performance Rechargeable Batteries. *Prog. Mater. Sci.* **2017**, *90*, 1-44.
- (11) Chan, M. K.; Wolverton, C.; Greeley, J. First Principles Simulations of the Electrochemical Lithiation and Delithiation of Faceted Crystalline Silicon. *J. Am. Chem. Soc.* **2012**, *134*, 14362-14374.
- (12) Liu, N.; Lu, Z. D.; Zhao, J.; McDowell, M. T.; Lee, H. W.; Zhao, W. T.; Cui, Y. A Pomegranate-Inspired Nanoscale Design for Large-Volume-Change Lithium Battery Anodes. *Nat. Nanotechnol.* **2014**, *9*, 187-192.
- (13) Hiu, X. H.; Zhong, L.; Huang, s.; Mao, S. X.; Zhu, T.; Huang, J. Y. Size-Dependent Fracture of Silicon Nanoparticles During Lithiation. *ACS Nano* **2012**, *6*, 1522-1531.
- (14) Sandu, I.; Moreau, P.; Guyomard, D.; Brousse, T.; Roue, L. Synthesis of Nanosized Si Particles via a Mechanochemical Solid-Liquid Reaction and Application in Li-Ion Batteries. *Solid State Ion.* **2007**, *178*, 1297-1303.
- (15) Chan, C. K.; Peng, H. L.; Liu, G.; McIlwrath, K.; Zhang, X. F.; Huggins, R. A.; Cui, Y. High-Performance Lithium Battery Anodes Using Silicon Nanowires. *Nat. Nanotechnol.* **2008**, *3*, 31-35.
- (16) Chan, C. K.; Patel, R. N.; O'Connell, M. J.; Korgel, B. A.; Cui, Y. Solution-Grown Silicon Nanowires for Lithium-Ion Battery Anodes. *ACS Nano* **2010**, *4*, 1443-1450.
- (17) Peng, K. Q.; Jie, J. S.; Zhang, W. J.; Lee, S. T. Silicon Nanowires for Rechargeable Lithium-

Ion Battery Anodes. *Appl. Phys. Lett.* **2008**, *93*, No. 033105.

(18) Yoo, J. K.; Kim, J.; Jung, Y. S.; Kang, K. Scalable Fabrication of Silicon Nanotubes and Their Application to Energy Storage. *Adv. Mater.* **2012**, *24*, 5452-5456.

(19) Ahn, J.; Lee, K. J.; Bak, W.; Kim, J.-J.; Lee, J.-K.; Yoo, W. C.; Sung, Y.-E. Elucidating Relationships between Structural Properties of Nanoporous Carbonaceous Shells and Electrochemical Performances of Si@Carbon Anodes for Lithium-Ion Batteries. *J. Phys. Chem. C* **2015**, *119*, 10255-10265.

(20) Liu, N.; Wu, H.; McDowell, M. T.; Yao, Y.; Wang, C. M.; Cui, Y. A Yolk-Shell Design for Stabilized and Scalable Li-Ion Battery Alloy Anodes. *Nano Lett.* **2012**, *12*, 3315-3321.

(21) Zhang, B.; Kang, F. Y.; Tarascon, J. M.; Kim, J. K. Recent Advances in Electrospun Carbon Nanofibers and Their Application in Electrochemical Energy Storage. *Prog. Mater. Sci.* **2016**, *76*, 319-380.

(22) Zhou, X. S.; Wan, L. J.; Guo, Y. G. Electrospun Silicon Nanoparticle/Porous Carbon Hybrid Nanofibers for Lithium-Ion Batteries. *Small* **2013**, *9*, 2684-2688.

(23) Ge, X. F.; Liu, S. H.; Qiao, M.; Du, Y. C.; Li, Y. F.; Bao, J. C.; Zhou, X. S. Enabling Superior Electrochemical Properties for Highly Efficient Potassium Storage by Impregnating Ultrafine Sb Nanocrystals within Nanochannel-Containing Carbon Nanofibers. *Angew. Chem. Int. Ed.* **2019**, *58*, 14578-14583.

(24) Park, S. W.; Shim, H. W.; Kim, J. C.; Kim, D. W. Uniform Si Nanoparticle-Embedded Nitrogen-Doped Carbon Nanofiber Electrodes for Lithium Ion Batteries. *J. Alloy. Compd.* **2017**, *728*, 490-496.

(25) An, G. H.; Ahn, H. J. Ultrafast Lithium Storage of High Dispersed Silicon and Titanium Oxide Nanoparticles in Carbon. *J. Alloy. Compd.* **2017**, *710*, 274-280.

(26) Chen, Y. L.; Hu, Y.; Shen, Z.; Chen, R. Z.; He, X.; Zhang, X. W.; Li, Y. Q.; Wu, K. S. Hollow Core-Shell Structured Silicon@carbon Nanoparticles Embed in Carbon Nanofibers as Binder-Free Anodes for Lithium-Ion Batteries. *J. Power Sources* **2017**, *342*, 467-475.

(27) Xu, Z. L.; Zhang, B.; Abouali, S.; Garakani, M. A.; Huang, J. Q.; Huang, J. Q.; Heidari, E. K.; Kim, J. K. Nanocavity-Engineered Si/Multi-Functional Carbon Nanofiber Composite Anodes with Exceptional High-Rate Capacities. *J. Mater. Chem.* **2015**, *2*, 17944-17951.

(28) An, G. H.; Kim, H.; Ahn, H. J. Improved Ionic Diffusion through the Mesoporous Carbon Skin on Silicon Nanoparticles Embedded in Carbon for Ultrafast Lithium Storage. *ACS Appl. Mater. Interfaces* **2018**, *10*, 6235-6244.

(29) Lai, F. L.; Zhou, G. Y.; Li, F.; He, Z. H.; Yong, D. Y.; Bai, W.; Huang, Y. P.; Tjiu, W. W.; Miao, Y. E.; Pan, B. C. Liu, T. X. Highly Dual Heteroatom-Doped Ultrathin Carbon Nanosheets with Expanded Interlayer Distance for Efficient Energy Storage. *ACS Sustain. Chem. Eng.* **2018**, *6*, 3143-3153.

(30) Zhang, X. S.; Zhou, L.; Zhang, Y.; Yan, S. R.; Huang, J. J.; Fang, Z. B. A Facile Method to Fabricate a Porous Si/C Composite with Excellent Cycling Stability for Use as the Anode in a Lithium Ion Battery. *Chem. Commun.* **2019**, *55*, 13438-13441.

(31) Zhou, G. M.; Tian, H. Z.; Jin, Y.; Tao, X. Y.; Liu, B. F.; Zhang, R. F.; Seh, Z. W.; Zhuo, D.; Liu, Y. Y.; Sun, J.; Zhao, J.; Zu, C. X.; Wu, D. S.; Zhang, Q. F.; Cui, Y. Catalytic Oxidation of Li<sub>2</sub>S on the Surface of Metal Sulfides for Li-S Batteries. *Proc. Natl. Acad. Sci.* **2017**, *114*, 840-845.

(32) Yao, Z. Y.; Yin, H. Y.; Zhou, L. M.; Pan, G. X.; Wang, Y. D.; Xia, X. H.; Wu, J. B.; Wang, X. L.; Tu, J. P. Ti<sup>3+</sup> Self-Doped Li<sub>4</sub>Ti<sub>5</sub>O<sub>12</sub> Anchored on N-Doped Carbon Nanofiber Arrays for Ultrafast Lithium-Ion Storage. *Small* **2019**, *15*, No. 1905296.

(33) Kim, S.-J.; Kim, M.-C.; Han, S.-B.; Lee, G.-H.; Choe, H.-S.; Kwak, D.-H.; Choi, S.-Y.; Son, B.-G.; Shin, M.-S.; Park, K.-W. 3D Flexible Si Based-Composite (Si@Si<sub>3</sub>N<sub>4</sub>)/CNF Electrode with Enhanced Cyclability and High Rate Capability for Lithium-Ion Batteries. *Nano Energy* **2016**, *27*, 545-553.

(34) Zhang, B.; Yu, Y.; Xu, Z. L.; Abouali, S.; Akbari, M.; He, Y. B.; Kang, F. Y.; Kim, J. K. Correlation Between Atomic Structure and Electrochemical Performance of Anodes Made from Electrospun Carbon Nanofiber Films. *Adv. Energy Mater.* **2014**, *4*, No. 1301448.

Table of Contents Graphic

